Genes & Diseases (2022) 9, 531–548

Available online at www.sciencedirect.com

ScienceDirect

journal homepage: http://ees.elsevier.com/gendis/default.asp

FULL LENGTH ARTICLE

Hypercalciuria switches Ca^{2+} signaling in proximal tubular cells, induces oxidative damage to promote calcium nephrolithiasis

Samuel Shin [1], Cliff-Lawrence Ibeh [1], Eugenia Awuah Boadi, Bok-Eum Choi, Sanjit K. Roy, Bidhan C. Bandyopadhyay*

Calcium Signaling Laboratory, Research Service, Veterans Affairs Medical Center, 50 Irving Street, NW, Washington, DC 20422, USA

Received 9 January 2021; received in revised form 5 April 2021; accepted 27 April 2021
Available online 15 May 2021

KEYWORDS
Apoptosis;
Ca^{2+}signaling;
Calcium nephrolithiasis;
Chronic kidney disease;
Fibrosis;
Hypercalciuria;
Inflammation;
Oxidative stress

Abstract Proximal tubule (PT) transports most of the renal Ca^{2+}, which was usually described as paracellular (passive). We found a regulated Ca^{2+} entry pathway in PT cells via the apical transient receptor potential canonical 3 (TRPC3) channel, which initiates transcellular Ca^{2+} transport. Although *TRPC3* knockout (−/−) mice were mildly hypercalciuric and displayed luminal calcium phosphate (CaP) crystals at Loop of Henle (LOH), no CaP + calcium oxalate (CaOx) mixed urine crystals were spotted, which are mostly found in calcium nephrolithiasis (CaNL). Thus, we used oral calcium gluconate (CaG; 2%) to raise the PT luminal $[Ca^{2+}]_o$ further in $TRPC3^{-/-}$ mice for developing such mixed stones to understand the mechanistic role of PT-Ca^{2+} signaling in CaNL. Expectedly, CaG-treated mice urine samples presented with numerous mixed crystals with remains of PT cells, which were pronounced in $TRPC3^{-/-}$ mice, indicating PT cell damage. Notably, PT cells from CaG-treated groups switched their mode of Ca^{2+} entry from receptor-operated to store-operated pathway with a sustained rise in intracellular $[Ca^{2+}]$ ($[Ca^{2+}]_i$), indicating the stagnation in PT Ca^{2+} transport. Moreover, those PT cells from CaG-treated groups demonstrated an upregulation of calcification, inflammation, fibrotic, oxidative stress, and apoptotic genes; effects of which were more robust in TRPC3 ablated condition. Furthermore, kidneys from CaG-treated groups exhibited fibrosis, tubular injury and calcifications with significant reactive oxygen species generation in the urine, thus, indicating *in vivo* CaNL. Taken together, excess PT luminal Ca^{2+} due to escalation of

Subject area: Hypercalciuria, Oxidative stress, Kidney Injury, Renal Pathology.

* Corresponding author. Fax: +(202) 462 2006.
E-mail address: bidhan.bandyopadhyay@va.gov (B.C. Bandyopadhyay).

Peer review under responsibility of Chongqing Medical University.

[1] These authors contributed equally.

https://doi.org/10.1016/j.gendis.2021.04.006

hypercalciuria in TRPC3 ablated mice induced surplus CaP crystal formation and caused stagnation of PT $[Ca^{2+}]_i$, invoking PT cell injury, hence mixed stone formation.

Introduction

The prevalence, incidence, and recurrence of calcium nephrolithiasis (CaNL) have been increasing worldwide due to changes in lifestyle, dietary habits, and environment.[1,2] The major problem in finding the exact pathogenesis of CaNL is that there is no established unified mechanism.[3] While there are arguments in finding the exact site of initial crystallization, clinical studies have been performed on kidney biopsies from stone patients.[4] However, the clinical manifestation had already been advanced in those samples where the anatomical site was determined.[4] Specifically, those are areas adjacent to the Randall's plaques in patients undergoing percutaneous nephrolithotomy, where large, complex crystals containing calcium phosphate (CaP) were detected at the basement membrane adjacent to loop of Henle (LOH). Evidently, the initial CaP (apatite) crystallization can be the root cause of CaP + calcium oxalate (CaOx) mixed stone formation in the distal part of the nephron with subsequent extension, and in more severe cases, to the papillae, which may have promoted heterogeneous nucleation, leading to CaNL.[5] Moreover, CaOx and/or CaP crystals can bind to the tubular epithelial cells, causing tissue injury, inflammation, and calcium biomineralization.[6–8] Recently, our *in vitro* study has found that such crystal injury to proximal tubular (PT) cells can cause store-operated Ca^{2+} entry (SOCE), leading to endoplasmic reticular (ER) stress induced cell death, due to the aberrant change in Ca^{2+} signaling pattern.[9] Such resultant cell death can accumulate cellular debris, containing lipids and proteins, which can promote calcium stone formation downstream.[10] Despite those harmful consequences, the relevance of such mechanism in a real-time *in vivo* condition, along with its implications in tubular nephropathy or in CaNL, are unclear.

Most stones in CaNL are made up of CaOx, where CaP has been found to be the core component,[3,11] and thus proposed as the nidus for CaP + CaOx mixed stone formation.[12] While the mechanism of such stone formation is unclear, nucleation of CaP crystals as the first event in this process is thought to begin at the thin descending limb of the LOH.[4] In this segment, tubular filtrate becomes concentrated, which makes it more prone to supersaturation, and it can be crystallized in presence of a higher pH of 7.4.[13–15] Thus, the regulation of Ca^{2+} transport upstream to LOH, i.e., in PT, could be critical in mitigating such downstream Ca^{2+} supersaturation and crystal formation.[13] PT handles the majority (~70%) of renal Ca^{2+} reabsorption,[16] which has been described as paracellular. However, our recent study indicated that a significant regulation of PT Ca^{2+} reabsorption via a transcellular pathway, comprised of Ca^{2+}-sensing receptor (CaSR) activated transient receptor potential canonical 3 (TRPC3), Ca^{2+} entry channel,[17] thus, can be a key mechanism to prevent CaP crystal formation immediately downstream at the LOH.

Defect in renal Ca^{2+} regulation,[18] due to idiopathic hypercalciuria, have been described to influence the filter load of Ca^{2+}. Although the dietary calcium intake was found to be inversely related to the risk of developing kidney stones,[19] evidence also indicates that the patients with idiopathic hypercalciuria may aggravate their condition by ingesting calcium supplements, and thereby increase their risk in developing calcium stones.[20] Interestingly, *TRPC3*$^{-/-}$ mice exhibited mild hypercalciuria, possibly due to the defect in PT Ca^{2+} reabsorption and CaP crystallization occurring at the luminal region of LOH.[17] Our rationale is to use *TRPC3*$^{-/-}$ mice as an initial simulated condition, where oral calcium gluconate (CaG) supplementation would be used to raise the tubular $[Ca^{2+}]$ even further, to enable us to follow real-time observation and understand the hypercalciuria-driven human-like manifestation of CaNL. CaG has a well-ionizing property,[21] hence it has been favored as a clinical supplementation of calcium.[22] In this manuscript, we presented the pathophysiology of mixed stone formation and uncovered the hypercalciuria-induced PT cells Ca^{2+} signaling signature that drives the expression profiles of new genes to regulate ROS-induced PT cell death. Such mechanism can facilitate mixed calcium stone formation in the downstream segments because preformed CaP crystals can bind with the cellular debris generated from those dead PT cells to augment the growth and aggregation of mixed crystals.

Material and methods

Animals

All animals used in this study were approved as part of a protocol designed in accordance with the Guiding Principles in the Care and Use of Animals, approved by the Institutional Animal Care and Use Committee (IACUC) and the Research and Development Committee of DC Veterans Affair Medical Center. Wild Type (WT) and *TRPC3* KO (−/−) mice purchased from the Jackson Laboratory (Bar Harbor, ME, USA) were maintained and crossed as described previously.[17,23] To induce hypercalciuria with 2% CaG plus 2% sucrose (as adjuvant), when supplemented to: WT mice denoted as WTT group and TRPC3 KO mice represented as KOT group. WT and TRPC3 KO mice treated with 2% sucrose alone were used as respective control to their CaG-treated counterpart. Documentation on calcium, food and water intake were recorded to determine any differences in dietary intake (calcium, food and water) between the treated and untreated groups.

Chemicals

Pyr3, NPS-2143, and SKF-96365 were purchased from Tocris Bioscience (Minneapolis, MN). 1-oleoyl-2-acetyl-sn-glycerol

(OAG), L-phenylalanine (L-Phe), Pyr6, Pyr10 and 2′,7′-dichlorodihydrofluorescein diacetate (H2DCFDA) were purchased from Sigma—Aldrich (St. Louis, MO, USA). Cell culture media, Dulbecco's modified Eagle's medium (DMEM), fetal bovine serum (FBS), antibiotics (penicillin and streptomycin), glutamine, and Fura-2-acetoxymethyl ester (Fura-2-AM) were purchased from Invitrogen (Carlsbad, CA, USA). ER tracker was purchased from Cell Signaling Technology (Danvers, MA, USA). All chemicals were analytical grade.

Mice urine electrolyte and pH measurements

For urine collection, each mouse was housed in individual metabolic cages (Nalgene, Rochester, NY, USA) with *ad libitum* food and water. For cages with treated mice, water contained 2% CaG (adjuvant with 2% sucrose) whereas 2% sucrose alone were used in their respective control cages. Both treated and untreated mice urine were collected (24 h), and urine pH was immediately measured using Orion Star A121 portable pH meter (Thermo Fisher Scientific, Waltham, MA, USA).[24] Urine and serum electrolytes (Na^+, K^+, and Cl^-) were measured using a Medica EasyLyte Analyzer (Bedford, MA, USA). Urine and serum Ca^{2+} were further measured using the Randox Calcium Assay Kit (Randox Laboratories, Kearneysville, WV, USA). QuantiChrom™ Phosphate Assay Kit (BioAssay Systems, Hayward, CA, USA) were used to determine urine and serum PO_4^{3-}. EnzyChrom™ Oxalate Assay Kit was used to measure urine oxalate (BioAssay Systems, Hayward, CA, USA). Serum parathyroid hormone (PTH) was measured using a mouse PTH EIA kit (RayBiotech Life, Norcross, GA, USA). Measurements of calcium, food and water intake were done to avoid confounding effect(s), if any.

Isolation and primary culture of PT cells

Renal PT cells were isolated from kidney cortical tissues of all treated and untreated mice to make primary cell preparation by enzymatic digestion, filtration and density gradient centrifugation as previously described.[17] These freshly dispersed preparations containing single cells and fragmented tubular structures of PT cells, were loaded with Ca^{2+} dye indicator (Fura-2-AM) for Ca^{2+} imaging experiments. In electrophysiological experiments, single cell preparations were used upon further purification. We have successfully characterized the purity of the PT cells genetically by discriminating with the presence of PT cell markers genes and absence of other tubular cells [thick ascending limb (TAL), distal tubule, collecting duct (CD) and intercalated (Fig. S1)], glomerular cells and blood vessels marker genes,[17] and functionally by Angiotensin II-mediated $[Ca^{2+}]_i$ increase and its blockade by losartan as described.[17,25] For Ca^{2+} imaging and electrophysiology experiments, we used both freshly dispersed and cultured cells as described previously.[17] Transwell filters (EMD Millipore, Burlington, MA, USA) were used for primary culture of PT cells for up to 3 days until they achieve confluency.

Time-lapse $[Ca^{2+}]_i$ fluorescence measurements

We performed time-dependent ratiometric (340/380 nm) $[Ca^{2+}]_i$ measurements of WT and *TRPC3* KO PT cells as previously described.[26] Cells that were loaded with Fura-2-AM were placed in a microincubator with the temperature set to 37 °C, and a gaseous mixture of 95% air and 5% CO_2 for the duration of the experiment. IX81 microscope images of the cells were taken using an IX81 motorized inverted microscope equipped with an IX2-UCB control box (Olympus USA, Center Valley, PA, USA). These images were fed into a C9100-02 electron multiplier CCD camera with an AC adaptor A3472-07 (Hamamatsu, Bridgewater, NJ, USA). We used a Lambda-LS xenon arc lamp and a 10—2 optical filter changer (Sutter Inst. Novato, CA, USA) as an illuminator which can output 340 and 380 nm to a 700 nm cutoff. The fluorescence emitted by Fura-2 was excited at wavelengths of 340 nm and 380 nm and emission was collected at wavelength of 500 nm. The PT cells were brought into focus by a differential interference contrast (DIC) channel. These measurements were digitally processed using the 3i Slidebook version 5.0 microscopy software (Intelligent Imaging Innovations, Denver, CO, USA). Time lapse was set at 400-500-time points at 1 s intervals in average of 50—150 cells for each experiment, where regions of interest were selected (background fluorescence automatically subtracted prior to 340/380 ratio calculation and graphing). Analysis was performed offline using Slidebook™ software (Olympus, Center Valley, PA, USA).

Electrophysiology

Ionic currents from single PT cells were measured using the whole-cell patch clamp technique as previously described.[17,27] Extracellular solution surrounding the cell was comprised of (in mM): 140 NaCl, 4 KCl, 1 $MgCl_2$, 2 $CaCl_2$, 5 D-glucose and 10 HEPES (NaOH, pH 7.4), whereas intracellular solution contained (in mM): 50 CsCl, 10 NaCl, 60 CsF, 20 EGTA, and 10 HEPES (CsOH, pH 7.2). Recordings of whole-cell were performed using EPC-10 digitally controlled amplifier and Patchmaster software (HEKA, Lambrecht, Germany). Data was obtained at 5.00 kHz and filtered at 2.873 kHz. Current—voltage (I—V) characteristic curve was ascertained every 3 s, by application of voltage ramps (300 ms) from −100 mV to +100 mV, with a holding potential of −80 mV. Once the whole-cell configuration has been established, series resistances >500 MΩ were used as standard. Room temperature set at 25 °C for the duration of the experiments.

RNA extraction, cDNA synthesis and polymerase chain reaction (PCR)

TRIzol was used to perform RNA extraction.[9,17] Briefly, cell pellets were lysed in TRIzol. RNA was separated in an aqueous phase after chloroform addition and then precipitated with 2-propanol followed by 75% ethanol. Precipitated RNA was air-dried and re-suspended in DEPC-treated water. Dissolved RNA was further purified using a DNase I,

Application Grade Kit (Sigma—Aldrich, St. Louis, MO, USA), as per the manufacturer's instructions. Purified RNA was quantified using a nanodrop spectrophotometer (ThermoFisher Scientific, Waltham, MA, USA) and used for cDNA synthesis. cDNA was prepared using GoScript™ Reverse Transcription System (Promega, Madison, WI, USA) as per the manufacturer's instructions. PCR Master mix was prepared using GoTaq® Green Master Mix (Promega, Madison, WI, USA) as per the manufacturer's protocol. 15 μL of master mix was added to 5 μL of cDNA template in 1:10 dilutions. List of primer sequences used in this study is shown in Table 1. Thermocycling parameters were: the initial denaturation at 95 °C for 3 min; subsequent PCR cycles (x35) of denaturation at 95 °C for 30 s, annealing at 55 °C for 30 s, and extension at 72 °C for 45 s; and a final elongation at 72 °C for 5 min.

Alizarin red staining of urine crystals and crystalized cells

Alizarin red (AR) staining was done as previously described to detect the presence of CaP and/or CaOx crystals in mice urine.[10,28,29] Briefly, urine was centrifuged; and the crystals with the cells were collected. Equal volumes of alizarin red stain pH 4.3 (for detection of only CaP crystals) or 6.8 (for detection of CaOx and mixed crystals) were added. Samples were then incubated at 37 °C for 30 min, and then centrifuged to remove the supernatant. Nest, crystal pellets were mounted on a slide for capturing images using light microscopy with Zeiss Axio Observer.Z1 Microscope. All stained images obtained using light microscopy were quantified using ImageJ as previously described.[10]

Urine lactate dehydrogenase (LDH) measurements

LDH present in all treated and untreated urine samples (6 h) were measured as an indicator of cell death induced cytotoxicity *in vivo* using Cytotoxicity Assay Kit (Promega, Madison, WI, USA) according to the manufacturer's instructions. Mice urine samples were aliquoted into a 96-well plate. Afterwards, the reaction mixtures were added to the corresponding wells. The mixtures were incubated for 60 min at room temperature without being exposed to light. To measure the fluorescence, excitation and emission wavelengths were set to 560 nm and 590 nm, respectively, with a SpectraMax M5e Multimode Microplate Reader (Molecular Devices, Sunnyvale, CA, USA). Absorbance values were quantitated with SoftMax Pro Software, version 5.4 (Molecular Devices, San Jose, CA, USA) and the values obtained with media were subtracted by those with the reagent only as previously described.[30]

Urine H_2O_2 measurements

To determine *in vivo* ROS generation, H_2O_2 in 6 h urine samples (released *in vivo*) from mice were assessed using H_2O_2 Cell-Based Assay Kit (Cayman Chemicals, Ann Arbor, MI, USA). Pre-assay and assay preparations were performed according to manufacturer's instructions. Extracellular H_2O_2 in media were assessed by subtracting the background wavelength (540 nm) from the emission wavelength at 590 nm.[30]

Histochemistry of kidney sections

Mice tissue sections (~5—7 μm) were prepared from whole kidneys collected from the all the mice groups after euthanasia, which were immediately fixed in 10% formalin solution for 24 h and then dehydrated in graded concentrations of ethanol and embedded in paraffin. Histochemistry was performed on paraffin sections of mice kidneys, as described previously.[17] Sections were stained with Hematoxylin and eosin (H&E), Masson or Alizarin Red pH 4.3 (for CaP crystal identification) or pH 6.8 (CaP and/or CaOx crystal identification) as described previously.[28,29,31] *In situ* apoptosis detections (Annexin V) were performed using TACS•XL®DAB *in situ* Apoptosis Detection Kit (Trevigen, Gaithersburg, MD, USA) on mice kidney tissue sections, as per manufacturer's instructions.

ER-tracker and H2DCFDA staining

ER stress in PT cells following CaSR activation and inhibition were measured by ER-Tracker™ Green by live-cell imaging with excitation at 504 nm and emission at 511 nm using Zeiss LSM710 laser-scan fluorescence microscope as described previously.[9] Detection of ROS from PT cells following CaSR activation and inhibition were measured using a cell-permeable fluorescent probe H_2DCFDA. Briefly, PT cells were incubated with H2DCFDA (10 μM) in HBSS (Invitrogen) for 30 min at 37 °C. Later cells were washed with 1 × PBS and then imaged under laser-scan (confocal) fluorescence microscope (Zeiss LSM710; Carl Zeiss).

Statistical analysis

Experimental data were plotted, and curve-fitting was performed with Origin 6.1. The data were expressed as means ± SEM from at least four separate experiments as indicated in the figure legends. Statistical analyses were performed using Student's unpaired *t*-test (two-tailed), or ANOVA, as appropriate, in Origin 6.1. Statistically significant comparisons were accepted at $P < 0.05$.

Results

CaG-treated mice demonstrated hypercalciuria under normocalcemic conditions

Hypercalciuria is common among stone-formers and thus can be considered as a major risk factor for stone-formation.[18] Such condition can also trigger oxidative stress in tubular epithelial cells, which can play a major role in the manifestation of the disease.[32] We found that both WTT and KOT, exhibited more urine Ca^{2+} clearance (Fig. 1A, B) than their untreated counterparts (WT and KO), and thus can be considered as mimicking a severe-hypercalciuric condition, while serum Ca^{2+} remained relatively similar between all groups (Fig. 1C). Furthermore, the ablation of TRPC3 exacerbated the urinary Ca^{2+} clearance, suggesting

Table 1 List of primers.

Primer	Sequence (sense, antisense)	Product Size (bp)
mGAPDH	5′-ACTCCACTCACGGCAAATTC-3′ 5′-TCTCCATGGTGGTGAAGACA-3′	171
mTRPC3	5′- TTCATGTTCGGTGCTCGTG-3′ 5′- TTTGTGCCCGTGTCTTTC-3′	831
mNCX1	5′-CCTTGTGCATCTTAGCAATG-3′ 5′-TCTCACTCATCTCCACCAGA-3′	437
mPMCA1	5′- TGGCAAACAACTCAGTTGCATATAGTGG- 3′ 5’ -TCCTGTTCAATTCGACTCTGCAAGCCTCG- 3′	562
mCaBp9	5′-GATCATAGTGGGTTTCAGG-3′ 5′-ATCGCCATTCTTATCCAG- 3′	326
mCalBp28	5′-TGGCATCGGAAGAGCAGCAG-3′ 5′-TGACGGAAGTGGTTACCTGGAAG-3′	210
mMegalin	5′-GTTCGGGTTGATGTTCTGGA -3′ 5′- ACTTGGGTAAGCCAGGGGTT-3′	369
mCD13B	5′-TCACAGTGATAACGGGAAAGCCCA -3′ 5′-ATAAGCTCCGTCTCAGCCAATGGT -3′	799
mCaSR	5′-AAACACCTACGGCACCTGAA-3′ 5′-TTGTAGTACCCAACTTCCTTGAACA-3′	152
mCLDN14	5′-ACCCTGCTCTGCTTATCC -3′ 5′-GCACGGTTGTCCTTGTAG-3′	131
mSMa	5′- AGATTGTCCGTGACATCAAGG -3′ 5′- TTGTGTGCTAGAGGCAGAGC-3′	538
mNBCe1	5′-CACTGAAAATGTGGAAGGGAAG-3′ 5′-TTATCACCCTTGTGCTTTGC-3′	544
mNaPiIIa	5′-AGACACAACAGAGGCTTC-3′ 5′-CACAAGGAGGATAAGACAAG-3′	181
mCHOP	5′- GAGCACTGGAATGTCATCTCGC-3′ 5′- AAGCATACAGGCAGTCAGCCTCC-3′	419
mBMP2	5′-TGGAAGTGGCCCATTTAGAG-3′ 5′-TGACGCTTTTCTCGTTTGTG-3′	166
mBMP6	5′- CCCGCCCGGAGTAGTTTTAGC-3′ 5′- AGTGCCCTTCTCCCCTCCATT-3′	168
mBMP7	5′- TACGTCAGCTTCCGAGACCT-3′ 5′- GGTGGCGTTCATGTAGGAGT-3′	117
mOCL	5′- CTGACAAAGCCTTCATGTCCAA-3′ 5′- GCGCCGGAGTCTGTTCACTA-3′	59
mOPN	5′- GATGATGATGACGATGGAGACC-3′ 5′- CGACTGTAGGGACGATTGGAG-3′	148
mRUNX2	5′- CGGCCCTCCCTGAACTCT-3′ 5′- TGCCTGCCTGGGATCTGTA-3′	75
mTGFb1	5′- CTGAGTGGCTGTCTTTTG-3′ 5′- TTGCTGTACTGTGTGTCC-3′	436
mFN1	5′- TGCACGATGATATGGAGAGC-3′ 5′- TGGGTGTCACCTGACTGAAC-3′	93
mNLRP3	5′-AGAGCCTACAGTTGGGTGAAATG-3′ 5′-CCACGCCTACCAGGAAATCTC-3′	116
mIL-1β	5′- TCCATGAGCTTTGTACAAGGA-3′ 5′- AGCCCATACTTTAGGAAGACA-3′	343
mIL-6	5′-TGGAGTCACAGAAGGAGTGGCTAAG-3′ 5′-TCTGACCACAGTGAGGAATGTCCAC-3′	155
mMCP1	5′- AGAGAGCCAGACGGGAGGAA-3′ 5′- GTCACACTGGTCACTCCTAC-3′	520
mNF-κβ	5′- GTGGAGGCATGTTCGGTAGT-3′ 5′- AGCTGCAGAGCCTTCTCAAG-3′	367
mGPX3	5′-TGGCTTGGTCATTCTGGGC-3′ 5′-CCCACCTGGTCGAACATACTT-3′	103

(*continued on next page*)

Table 1 (*continued*)

Primer	Sequence (sense, antisense)	Product Size (bp)
m18S	5′-ACGGAAGGGCACCACCAGGA-3′ 5′-CACCACCACCCACGGAATCG-3′	127
mBax1	5′- GAGACACCTGAGCTGACCTT-3′ 5′- GCACCAGTTTGCTAGCAAAG-3′	244
mBCL2	5′- CTCGTCGCTACCGTCGTGACTTCG -3′ 5′- CAGATGCCGGTTCAGGTACTCAGTC -3′	242
mCaspase3	5′- AGAGAGCCAGACGGGAGGAA-3′ 5′- GTCACACTGGTCACTCCTAC-3′	519
mKIM1	5′-ATGAATCAGATTCAAGTCTTC-3′ 5′-TCTGGTTTGTGAGTCCATGTG-3′	548
mClaudin 2	5′-TGCGACACACAGCACAGGCATCAC-3′ 5′-TCAGGAACCAGCGGCGAGTAGAA-3′	300
mAqp 1	5′- CATCACCTCCTCCCTAGTC-3′ 5′- CATGCGGTCTGTGAAGTCG-3′	385
mAqp 2	5′-GCCATCCTCCATGAGATTACC-3′ 5′-ACCCAGTGATCATCAAACTTG-3′	305
mNKCC2	5′-AACTCAGTGCCCAGTAGTGC-3′ 5′-AGGCATCCCATCTCCATTAG-3′	429

that the urinary conditions could be more susceptible to Ca^{2+} stone formation (Fig. 1B). An assessment of the dietary intake of both food and water among the mice groups (WT, WTT, KO and KOT) were measured, which showed that there are no significant differences between the groups (Fig. S2), thus eliminating the possibility of any confounding effects. Importantly, other urinary and serum ions measured (Na^+, K^+, Cl^- and $C_2O_4^{2-}$) did not exhibit significant changes between the mice groups (Fig. 1F—L) due to CaG treatment except for urinary PO_4^{3-} which was decreased in the treatment group despite serum PO_4^{3-} remaining relatively the same for both the treated and untreated groups (Fig. 1D, E). This observation could be due to the increased formation of CaP crystals in the treated groups (WTT and KOT) following the increased availability of luminal Ca^{2+} in hypercalciuric conditions. Similarly, urinary pH and volume were not affected due to CaG treatment (Fig. 1M, N), eliminating the effect of pH on CaSR activation. Serum PTH levels did not change between the groups (WT, WTT, KO and KOT; Fig. S3), indicating the involvement of PTH-independent pathway in regulating PT luminal $[Ca^{2+}]_o$.[33]

TRPC3 plays a critical role in preventing stone-forming phenotype

Since ablation of TRPC3 can induce CaP urine crystals formation,[17] we determined if further elevation of luminal $[Ca^{2+}]_o$ can stimulate CaP + CaOx crystal formation (Fig. 2A). As expected, urine from our CaG-treated groups contained significant amount of CaP crystals, in which KOT urine contained highest number of crystals compared to any other group (Fig. 2B). We found similar trends in mixed CaP + CaOx crystals formation, where KOT marked the highest (Fig. 2C). More importantly, urines from both treated groups displayed numerous cells, in which some are calcified, compared to the KO and WT counterparts (Fig. 2B—D). To identify the origin of these cells and to ascertain why they were significantly present in our treated mice urine (WTT and KOT), we performed gene expression analysis on those urine cells. We found that these cells expressed CD13 and Megalin (Fig. 2E) and Kidney Injury Molecule 1 (KIM1; Fig. 2F), which suggests *in vivo* PT cell damage[34] and that PT cells in *TRPC3*$^{-/-}$ mice become more susceptible to injury due to hypercalciuric stress. Our most significant finding is that the presence of H_2O_2 in CaG-treated mice urine (Fig. 2G), which is the indication of *in vivo* ROS production. Notably, KOT group exhibited greater H_2O_2 levels, which could have triggered the cell death since the urine LDH levels were also found to be higher than their untreated counterparts (Fig. 2H), suggesting the extent of *in vivo* cytotoxicity due to hypercalciuria.

CaG-induced hypercalciuria evoked sustained $[Ca^{2+}]_i$ rise in PT cells

We used CaG to elevate PT luminal $[Ca^{2+}]_o$ to understand the Ca^{2+} signaling mechanism operated *in vivo* during elevated-hypercalciuric condition using WT-treated (WTT) and TRPC3 KO-treated (KOT) mice (Fig. 3A). Ca^{2+} transients were measured in Fura-2-AM loaded cells, which were utilized as indirect measurements of the behavior of Ca^{2+} influx and efflux from PT cells.[35,36] While the CaSR-induced Ca^{2+} response in WT PT cells was short-lived (Fig. 3B), Ca^{2+} entry into WTT PT cells was significantly greater in peak Ca^{2+} response (entry) with a prolonged Ca^{2+} transient (Fig. 3C). Remarkably, CaSR activated PT cells from KO groups induced a shorter peak Ca^{2+} entry compared to the WT counterpart (Fig. 3B, D).[17] More importantly, Ca^{2+} influx was further pronounced in KOT PT cells (Fig. 3E) upon L-Phe-induced CaSR activation compared to the WTT group, which may be due to the slowdown in Ca^{2+} mobilization from apical to basal end in absence of TRPC3. A graphical representation of all peak Ca^{2+} entries, rise, and decline were compiled in Figure 3F—H. Significantly, we observed a

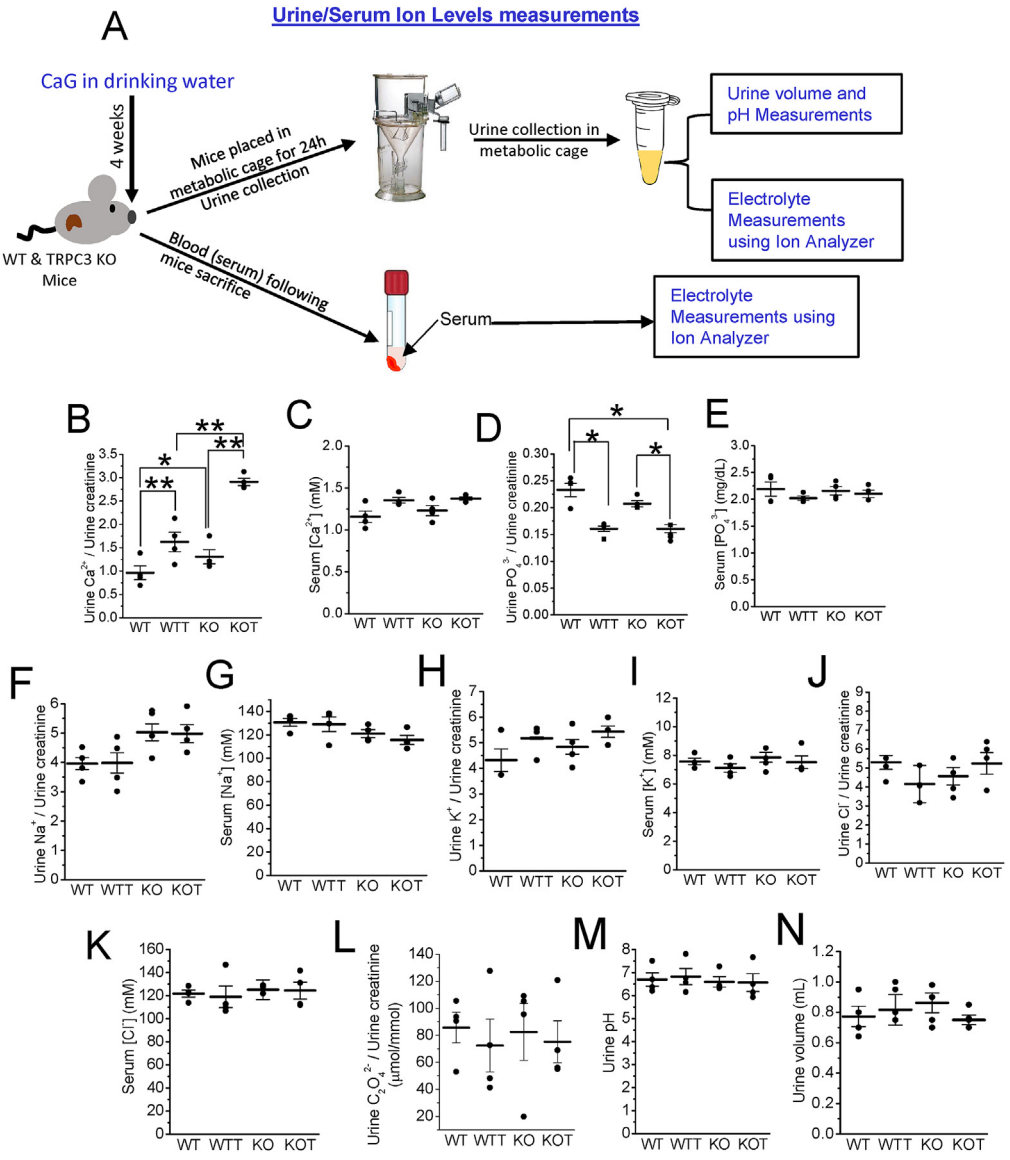

Figure 1 CaG-induced greater hypercalciuric response to exacerbate urinary Ca^{2+} clearance. **(A)** Experimental diagram depicts the process of urine and serum collection with subsequent electrolyte measurements. Serum and urinary electrolyte levels of **(B, C)** Ca^{2+}, **(D, E)** PO_4^{3-}, **(F, G)** Na^+, **(H, I)** K^+, **(J, K)** Cl^-, and $C_2O_4^{2-}$ **(L)** from 24-hr urine collection at the end of CaG treatments (4 weeks) from WT, WT CaG-treated (WTT), TRPC3 KO (KO), and KO CaG-treated (KOT) mice. All ion measurements were normalized to creatinine. **(M)** Urine pH and **(N)** volume measurements were performed immediately after 24 h urine collection. **(B)** Urinary Ca^{2+} clearance was significantly higher in our treated group, particularly for the KOT group. **(C)** Serum Ca^{2+} on the other hand did not change between the untreated and treated groups. **(D)** Urine PO_4^{3-} clearance reduced with treatment, showing an inverse correlation with urinary Ca^{2+} clearance. **(E)** Serum PO_4^{3-} remained stable between untreated and treated groups with no significant difference between the groups. Urine Na^+, K^+, Cl^-, $C_2O_4^{2-}$ and pH measurements **(F, H, J, L, M)** and **(G, I, K)** serum Na^+, K^+, and Cl^- measurements were insignificant among the groups. **(B–L)** Scatter plots of electrolytes, pH, and volume are means ± SEM. Urine and serum were collected from $n = 4$ of each mice group (WT, WTT, KO, and KOT). *, $P < 0.05$; **, $P < 0.01$.

greater and prolonged rise of $[Ca^{2+}]_i$ in both WTT and KOT PT cells compared to WT and KO respectively (Fig. 3G). In-depth analysis of our data show: higher peak Ca^{2+} response (Fig. 3F), enhancement of total Ca^{2+} rise (Fig. 3G), and the stagnation of $[Ca^{2+}]_i$ mobilization, which may also be evidenced by reduced percent Ca^{2+} clearance (Fig. 3H) in both WTT and KOT PT cells. Together, these results suggest that because of overwhelming agonist (filtrate Ca^{2+} loads) present in WTT PT cells, there is a stagnation in $[Ca^{2+}]_i$, whereas in absence of TRPC3 (KOT) such effect was deteriorated, indicating the role of TRPC3 in preventing hypercalciuric surge in $[Ca^{2+}]_i$ and inefficient Ca^{2+} intake by PT cells. Since sustained rise in $[Ca^{2+}]_i$ promotes ROS generation and cellular injury,[10] our results may establish a Ca^{2+} signaling signature in PT cells during severe-hypercalciuria.

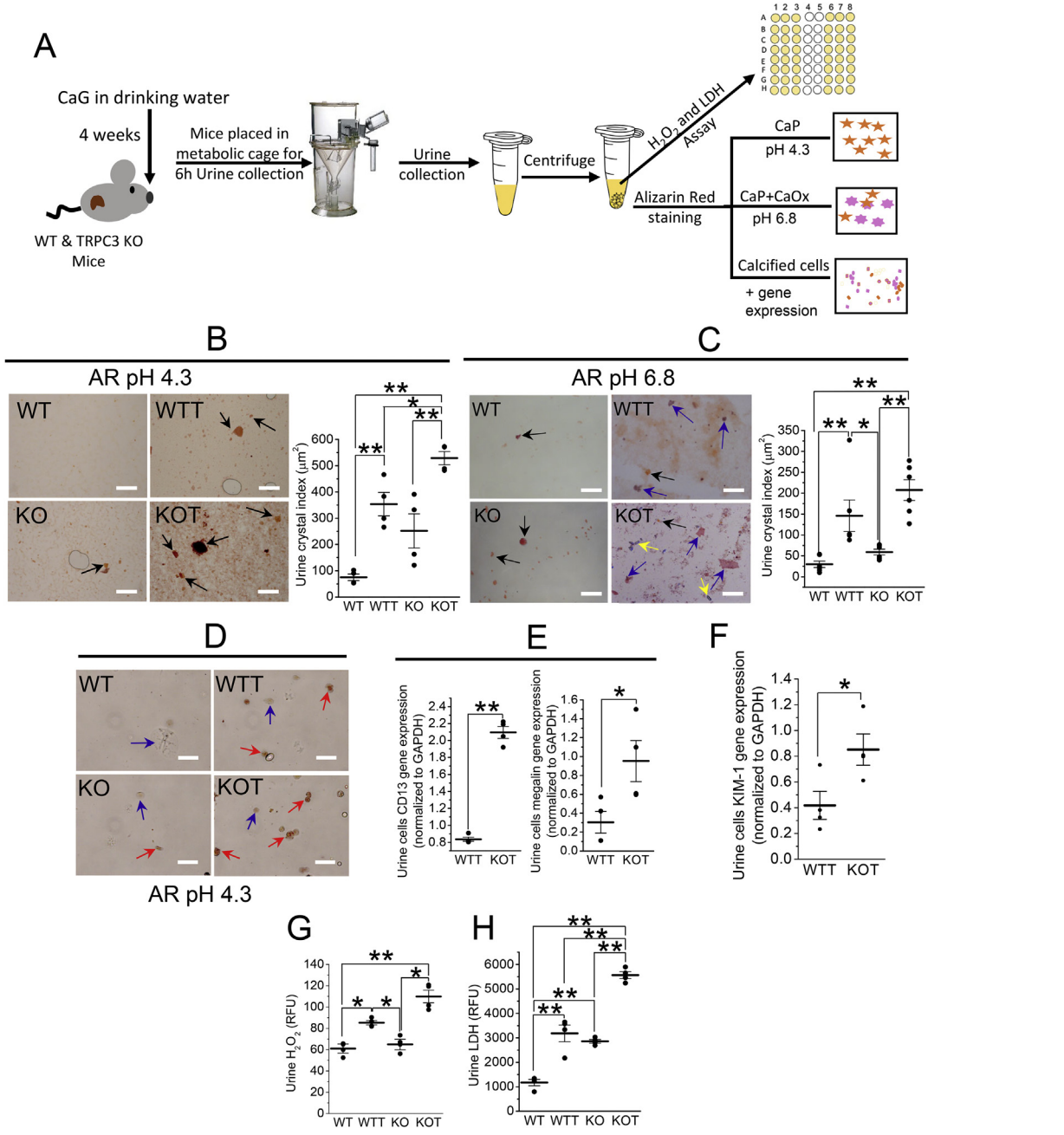

Figure 2 Hypercalciuria induced urine crystal formation, PT cell calcification and *in vivo* ROS generation. **(A)** Schematic presentation is showing the method of urine collection with successive urine staining, crystal detection, ROS and gene expressions measurements. Overnight urine collected from WT, WT CaG-treated (WTT), *TRPC3* KO (KO), and KO CaG-treated (KOT) mice stained with **(B)** Alizarin Red (AR) pH 4.3 (stains CaP crystals) and **(c)** pH 6.8 (stains both CaOx and CaP + CaOx crystals) to differentially visualize calcium crystals present in the urine. **(B)** While WTT mice presented significant CaP (black arrows) urine crystal formation, CaP crystal formation was higher in KOT mice urine; KO mice presented with fewer CaP crystals. **(C)** WTT and KOT mice urine showed significant mixed (CaP + CaOx; blue arrows) crystal formation, with few CaOx (yellow arrows) crystals. Comparatively fewer CaP (black arrows) crystals were found in WT and KO mice urine. **(D)** Calcified cells (red arrows) were detected in WTT and KOT mice urine by staining with AR 4.3. with normal (uncalcified) cells (blue arrows). **(E)** Origin of urine cells detected by the expression of PT markers genes (CD13 and Megalin), which were pronounced in the KOT groups (PT injury due to TRPC3 ablation). No other tubular marker genes were detected in those urine cells. (**F**) KIM-1 (kidney injury molecule 1) expression was found in those urine cells, which was significantly higher in KOT group compared to the WTT counterpart. **(G)** H_2O_2 releases were detected in the urine, which were higher in WTT and KOT PT group compared to the WT and KO group. **(H)** Similarly, LDH releases were examined in all mice urine; progressive increases have been found from KO, WTT and KOT groups. Scatter plots in **B, C, E, F, G, and H** are means ± SEM. *, $P < 0.05$; **, $P < 0.01$. Urine collected four times from $n = 4$ mice of each group (WT, WTT, KO, and KOT). White bars = 100 μm. All gene expressions were normalized to GAPDH.

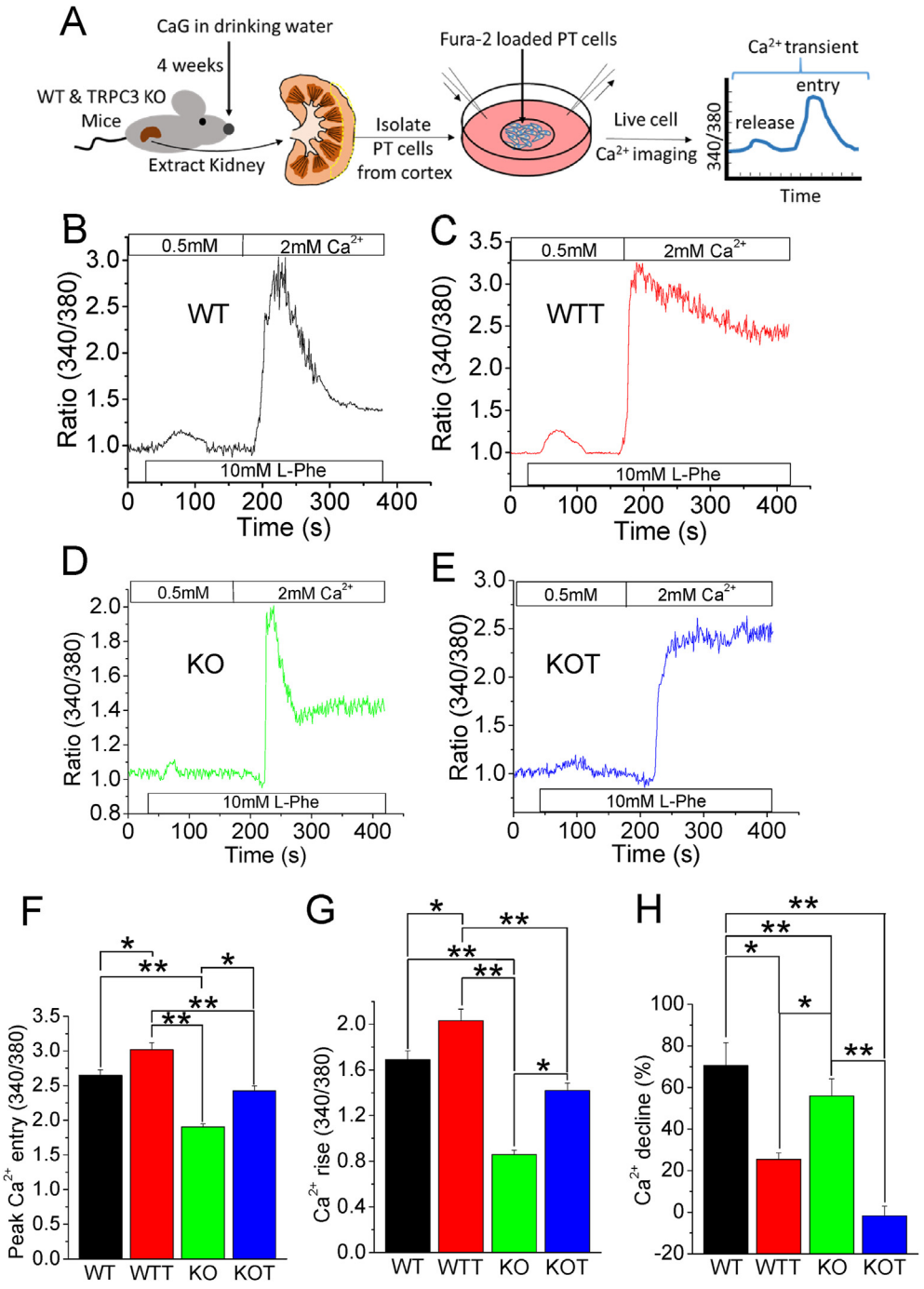

Figure 3 CaG treated WT and TRPC3 KO PT cells displays significant slowdown in $[Ca^{2+}]_i$ mobilization. (**A**) Experimental protocol for mice PT cell isolation and Ca^{2+} imaging. Mean Fura-2 fluorescence ratio (340/380 nm) obtained from Ca^{2+} imaging experiments in PT cells isolated from **(B)** WT, **(C)** CaG-treated WT (WTT), **(D)** *TRPC3* KO (KO), or **(E)** CaG-treated KO (KOT) mice. Average Ca^{2+} transient (**B**—**E**) are showing activation of CaSR by L-Phe (10 mM) in presence of 0.5 mM Ca^{2+} bath solution, then replenished with Ca^{2+} (2 mM). Attenuation of $[Ca^{2+}]_i$ mobilization in TRPC3 KO PT cells (compared to WT) is further intensified in **(C)** WTT and **(E)** KOT cells. Bar diagrams represent **(F)** peak Ca^{2+} entry, which represents the absolute amount of Ca^{2+} entering the cell after replenishing $[Ca^{2+}]_o$ in physiological condition, right before the $[Ca^{2+}]_i$ is dissipated or extruded from the cell **(G)** overall $[Ca^{2+}]_i$ rise, which is calculated by subtracting baseline $[Ca^{2+}]_i$ from the peak Ca^{2+} entry and **(H)** percent decline of Ca^{2+} from **(B**—**E)**, is the Ca^{2+} decay, as an indirect measurement of Ca^{2+} efflux, which is calculated by dividing Ca^{2+} entry (50 s after peak Ca^{2+} entry), over the Ca^{2+} rise, then multiplying by 100. This graphical representation shows the stagnation of $[Ca^{2+}]_i$ mobilization in CaG-treated TRPC3 KO PT cells (**F**—**H**). Peak responses were calculated from 50 to 150 cells on $n = 4$ of each mice group (WT, WTT, KO, and KOT). Bar diagrams are in means ± SEM. *, $P < 0.05$; **, $P < 0.01$.

Change in sensitivity of TRPC3 and CaSR in hypercalciuric conditions

To further confirm the changes in behavior of PT cell Ca^{2+} signaling signature in presence of TRPC3 in hypercalciuria, we evoked a TRPC3 current by OAG (100 μM; DAG analog) and its blockage by Pyr3 (TRPC3 inhibitor) in WT and WTT PT cells (Fig. 4A–E).[17,37] Since the WTT PT cells exhibited an outwardly rectifying current like its untreated counterpart (Figs. 4B),[17] the OAG elicited current was almost completely blocked by Pyr3 (Fig. 4C, E), confirming direct activation of TRPC3 in WTT PT cells.[37] Notably, the current activation of TRPC3 by OAG was shown to be higher in WTT than WT PT cells (Fig. 4D), while there was no difference in Pyr3 inhibition (Fig. 4E). In KOT PT cells, Pyr3 did not block the remaining CaSR-induced current, confirming our negative control (Data not shown). We examined the residual current in KOT PT cells by activating CaSR and found a steady rise in the current-ramp traces at +100 mV (Fig. 4F, G). Interestingly, the current induced by L-Phe was greater in TRPC3 KOT PT cells than that of KO PT cells by a factor of about three (Fig. 4H). To confirm the activation of CaSR, we applied a known CaSR inhibitor, NPS-2143 (1 μM)[38] which inhibited ~80% of the induced current in both *TRPC3*-KO and *TRPC3* KOT PT cells (Fig. 4I). Altogether, these results suggest that in the absence of TRPC3, mass CaSR-activation in PT cells may have been hindered, even after hypercalciuric conditions. However, TRPC3 remains to be a major component in CaSR-induced signaling pathway in WTT PT cells in relatively mild hypercalciuric conditions, which could potentially prevent further rise in $[Ca^{2+}]_i$ and provide protection towards ROS generation.

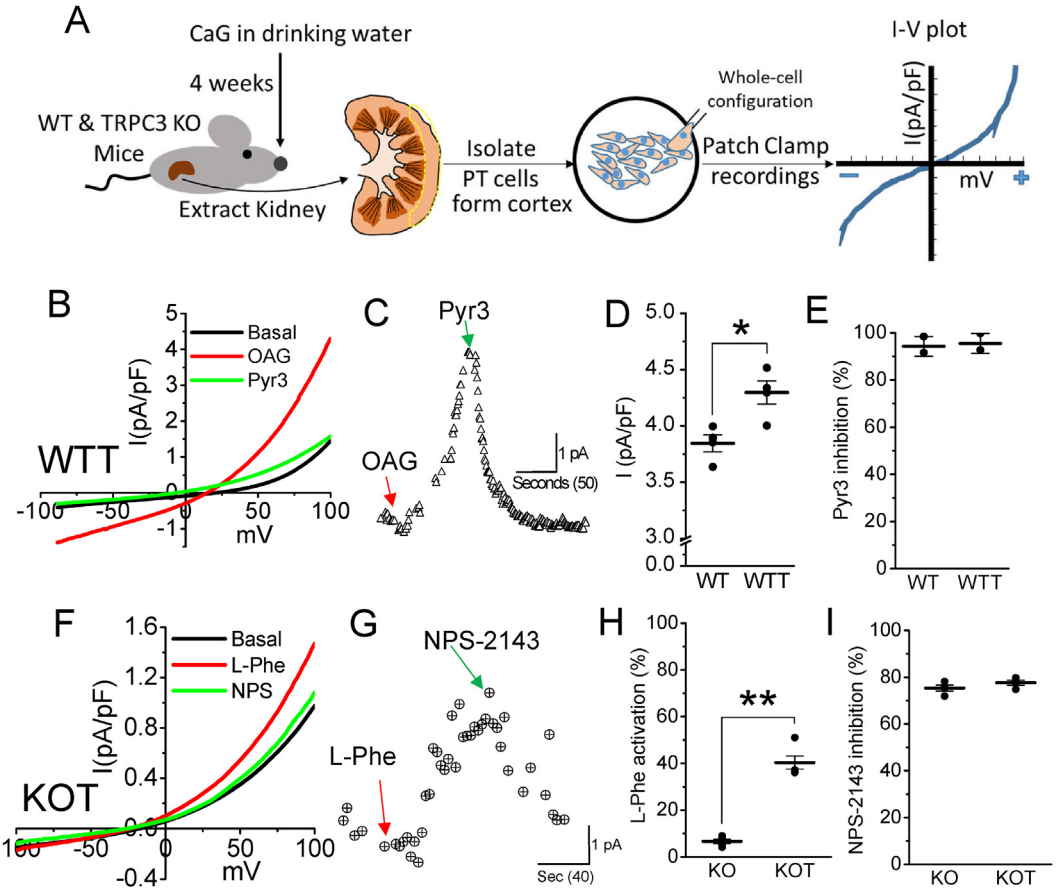

Figure 4 Induced-hypercalciuria displays the rise in TRPC3-activated current in mice PT cells. **(A)** Methodology of electrophysiological experiments. (**B**) Average I–V curve ploted from whole cell current in PT cells from CaG-treated WT (WTT) mice depicting an outwardly rectified current obtained after voltage ramping from −100 to +100 mV followed by exposure to OAG (100 μM) and TRPC3 inhibitor Pyr3 (1 μM). **(C)** Graphical current traces of average data; from (B), plotted as time course at +100 mV. WTT mice PT cells displayed an immediate stimulation upon application of OAG with a steep rise of the current ramp trace. Average data presented as scatter plots of **(D)** current densities (pA/pF) due to OAG-activation and **(E)** inhibition by Pyr3 in WTT PT cells compared to WT counterpart **(F)** I–V curve plotted from average current data representing an outwardly rectified current, typical of TRPC channel in PT cells from KO-CaG-treated (KOT) mice after voltage ramping from −100 to +100 mV followed by exposure to L-Phe and an allosteric CaSR inhibitor, NPS-2143 (1 μM). **(G)** Graphical representation of current traces from average data (F), represented as time course at +100 mV. Average scatter plots of percent **(H)** L-Phe activation and **(I)** NPS-2143 inhibition of KO and KOT PT cells. Scatter diagrams represent current measurements performed in separate experiments, $n = 4$ of each mice group (WT, WTT, KO, and KOT) with means ± SEM *, $P < 0.05$; **, $P < 0.01$.

Induced-hypercalciuria switches the mode of CaSR activated Ca^{2+} entry

Similar to other epithelial cells, we found that CaSR-activated PT cells trigger receptor operated Ca^{2+} entry (ROCE) under normal physiological condition,[17] whereas dysregulation of Ca^{2+} homeostasis in PT cells undergo endoplasmic reticulum (ER)-stress which was coupled with SOCE.[9,39] Thus, to discriminate the mode of Ca^{2+} entry after CaSR-activation in severe-hypercalciuric conditions, we performed Fura-2 measurements of WT, WTT, KO, and KOT PT cells with various inhibitors (Fig. 5A). WT PT cells exhibited the expected inhibition of Ca^{2+} entry by Pyr3 (3 μM) and SKF-96365 (10 μM; TRPC channel blocker),[40] whereas 2-APB (12 μM), an IP_3 receptor inhibitor,[41] only modestly blocked the Ca^{2+} entry (Fig. 5B). In WTT PT cells, Pyr3 and SKF-96365 inhibitions were significant, but 2-APB also had a noteworthy inhibition of the Ca^{2+} entry (Fig. 5C), revealing a potentially expanded role of ER-store release in Ca^{2+} entry. In KO PT cells, 2-APB significantly inhibited more of the CaSR-induced Ca^{2+} entry than SKF-96365 (Fig. 5D), which could be due to non-TRPC3 mediated Ca^{2+} entry by CaSR.[17] Interestingly, in KOT PT cells, both SKF-96365 and 2-APB did not significantly inhibit the Ca^{2+} entry (Fig. 5E), suggesting that the IP_3-R-induced SOCE may have been diminished. Furthermore, to understand the mechanism of CaSR induced Ca^{2+} entry due to the hypercalciuric-stress in presence and absence of TRPC3, we blocked SOCE pathway by Pyr6 and ROCE pathway by Pyr10 (3 μM).[39] Pyr10 (3 μM) inhibition comparison revealed that the TRPC3 appears to be a greater factor in the contribution of ROCE than the treatment (Fig. 5F). Moreover,

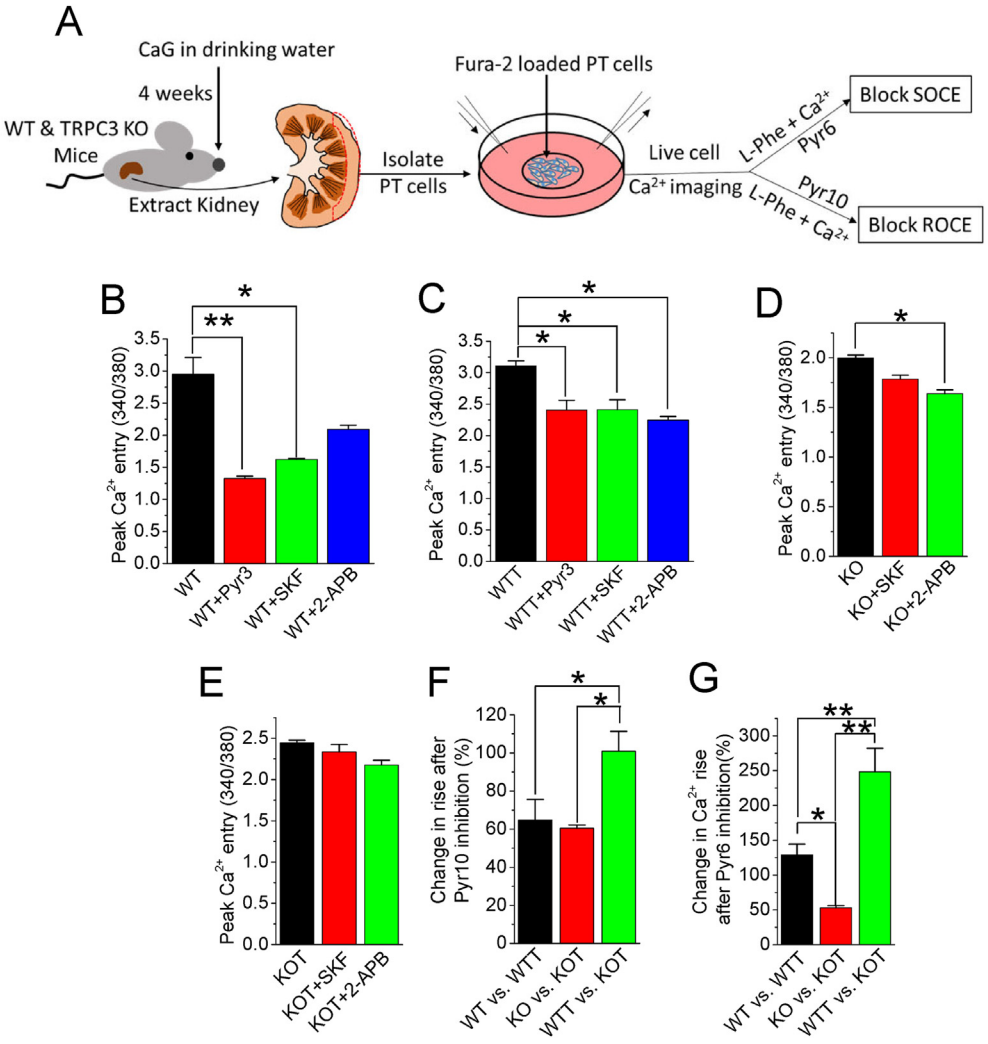

Figure 5 Mice PT cells due to induced-hypercalciuria switches the mode of Ca^{2+} entry to SOCE. **(A)** Schematics of PT cell isolation and Ca^{2+} imaging experiments. Bar diagrams represent average values of peak Ca^{2+} entry after L-Phe (10 mM) induced CaSR activation followed by Ca^{2+} (2 mM) replenishment in the presence of Pyr3, (3 μM) a TRPC3 inhibitor, SKF-96365 (10 μM), TRPC channel blocker, or 2-APB (12 μM), a SOCE blocker, in **(B)** WT, **(C)** WT CaG-treated (WTT), **(D)** *TRPC3* KO (KO), or **(E)** KO CaG-treated (KOT) PT cells. Bar graphs comparing percentage changes in Ca^{2+} rise between WT *vs.* WTT, KO *vs.* KOT, or WTT *vs.* KOT using ROCE and SOCE pyrazole inhibitors, **(F)** Pyr10 or **(G)** Pyr6, respectively. Peak responses measured from 50 to 150 cells on $n = 4$ of each mice group (WT, WTT, KO, and KOT). Bar diagrams are in means ± SEM. *, $P < 0.05$; **, $P < 0.01$.

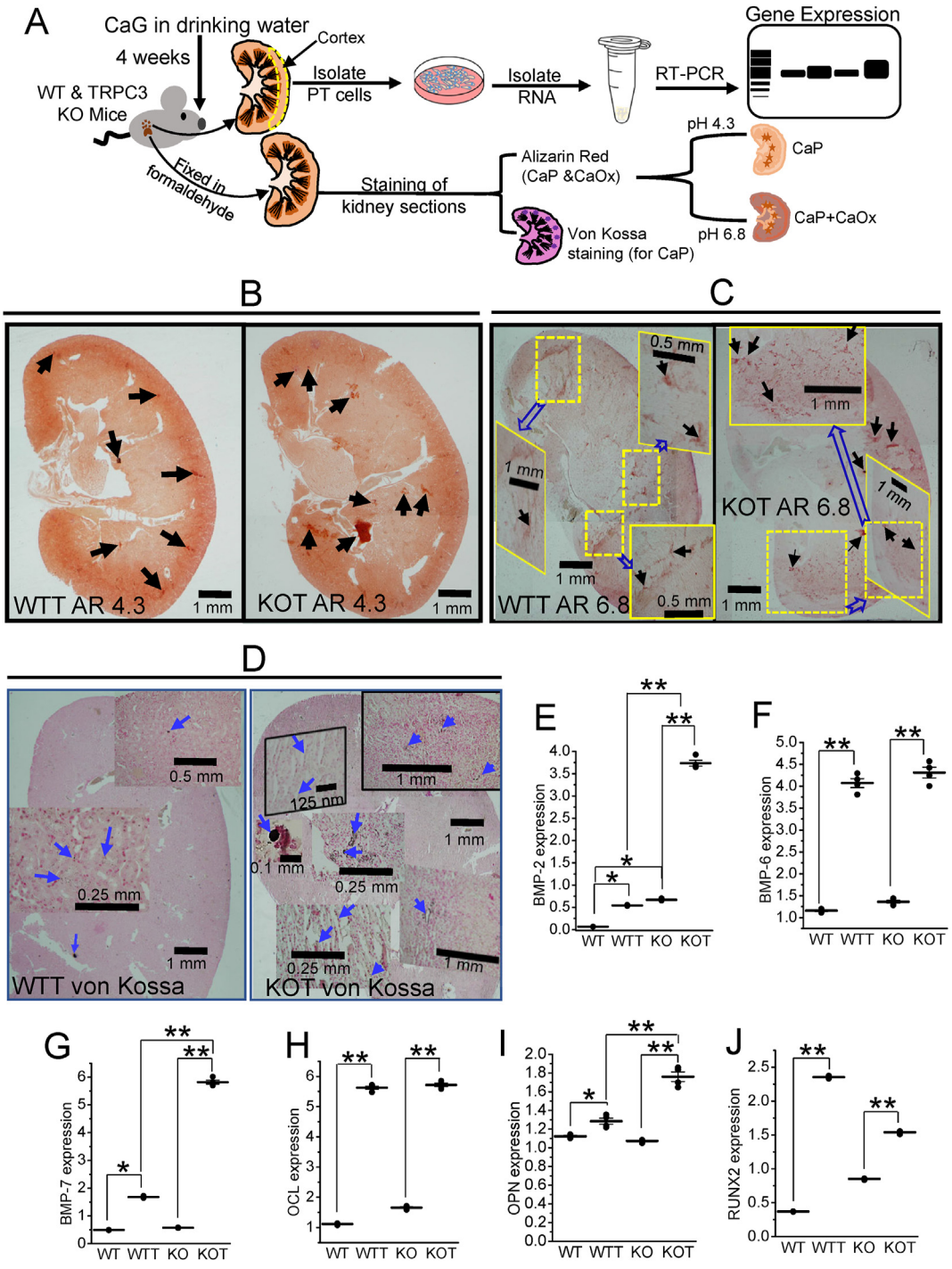

Figure 6 Histological characterization of CaNL phenotype during induced-hypercalciuria, presented with stone formation and calcification gene expression. **(A)** Method diagram represents RNA isolation from extracted PT cells and histological preparation of kidney sections. **(B, C)** Representative Alizarin Red (AR) staining of whole kidney sagittal sections of WT CaG-treated (WTT) and TRPC3 KO CaG-treated (KOT) shows calcified regions of the kidney. Black arrows show evidence of kidney stone areas within the section. AR pH 4.3 staining shows CaP stones present in the LOH region of whole kidney while AR pH 6.8 shows CaP + CaOx (mixed) stones in the calyx region of whole kidney. **(D)** Von Kossa staining of WTT and KOT kidney sections revealing areas of calcification deposits with blue arrows. Evidence of calcification in PT cells of treated mice are shown through quantification of gene expression profiles of known calcification markers; **(E)** BMP-2, **(F)** BMP-6, **(G)** BMP-7, are significantly higher for the treated groups especially for KOT compared to the controls (WT and KO), **(H)** OCL, **(I)** OPN, **(J)** RUNX2 show similar expression pattern to the BMPs in PT cells of WT, WTT, KO, and KOT. Kidneys for sectioning or RT-PCR were obtained from $n = 4$ mice of each group (WT, WTT, KO, and KOT). **(E–J)** Scatter plot quantifications are means ± SEM *, $P < 0.05$; **, $P < 0.01$. Scale bars are indicated in respective images. All gene expressions are normalized to GAPDH.

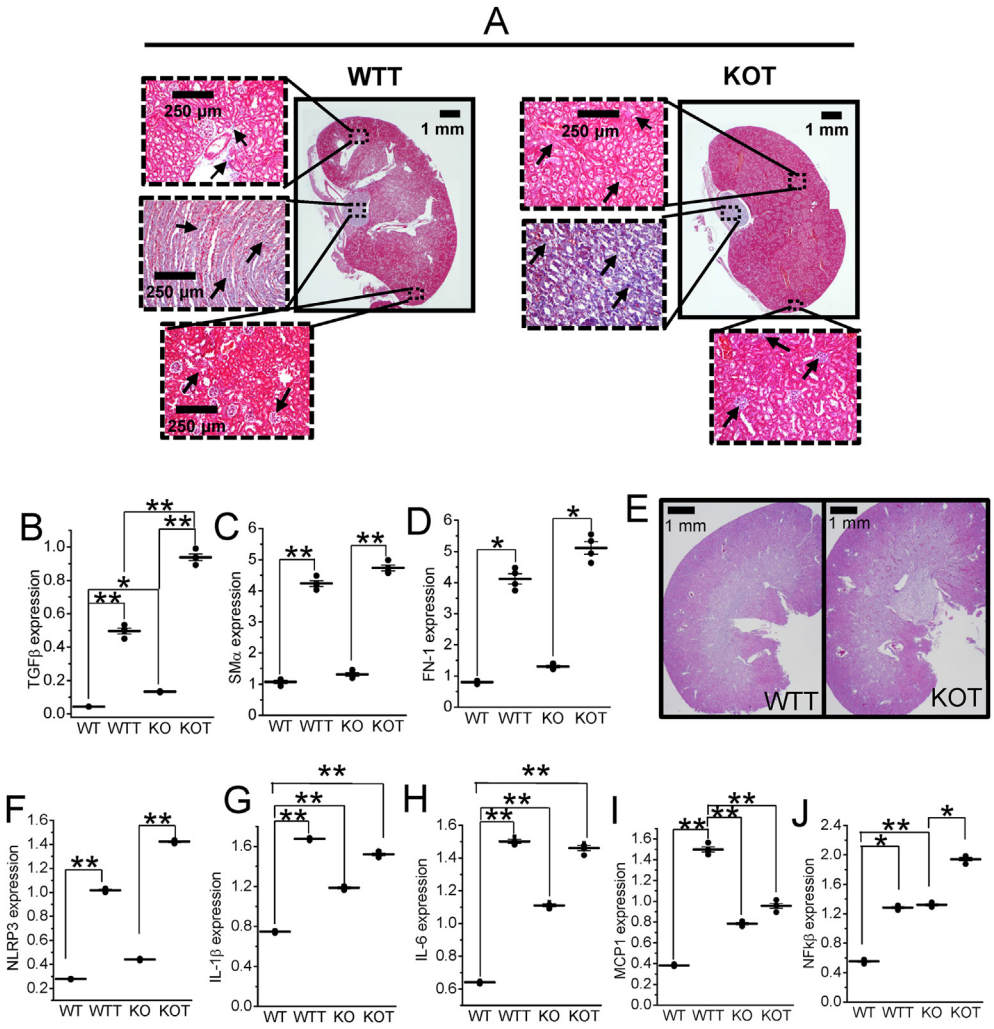

Figure 7 Histological and genetic characterization of Fibrosis and Inflammation following induced-hypercalciuria. **(A)** Kidney sagittal sections of WT CaG-treated (WTT) and TRPC3 KO CaG-treated (KOT) mice stained with Masson's Trichrome stain to assess fibrotic regions of the kidney; black arrows point to areas of fibrosis in the sagittal sections. Indication of renal fibrosis and inflammation are shown through gene expression levels for fibrotic marker genes **(B)** TGFβ, **(C)** SMα, and **(D)** FN-1 in WT, WTT, KO, and KOT mice PT cells are significantly higher for the treated groups especially for KOT compared to the controls. **(E)** Kidney sagittal sections of WTT and KOT stained with H&E to assess inflammatory regions of the kidney. Gene expression profiles of inflammatory markers **(F)** NLRP3, **(G)** IL-1β, **(H)** IL-6, **(I)** MCP1, and **(J)** NFκβ in WT, WTT, KO and KOT mice PT cells are significantly higher for the treated groups especially for KOT compared to the controls except for MCP1 which shows significant increase in expression only in WTT. Kidneys for sectioning or RT-PCR were obtained were obtained from $n = 4$ mice of each group (WT, WTT, KO, and KOT). Scatter plot quantifications in **(B–J)** are means ± SEM. *, $P < 0.05$; **, $P < 0.01$. All gene expressions are normalized to GAPDH.

inhibition by Pyr6 became more pronounced in KOT PT cells than that of WTT PT cells (Fig. 5G), indicating greater involvement of the SOCE pathway due to TRPC3 ablation. These results confirm that the majority of Ca^{2+} entry contribution in PT cells switches from ROCE to SOCE due to hypercalciuric-stress response in both presence/absence of TRPC3 (Fig. 5G).

Increased renal calcification in *TRPC3* KO mice in hypercalciuric conditions

Previous observations suggest an association between clinical condition of stone formation and calcification.[9,42] Since we found significantly greater crystalluria in the CaG-treated condition, we examined the degree of stone-formation and/or calcification *in vivo* within the kidneys of those treated groups (Fig. 6A). Our results show both CaP (shown with AR 4.3 stain) and CaP + CaOx crystals (shown with AR 6.8 stain) in kidneys of WT and KO mice were elevated after CaG treatment (Fig. 6B, C), evidenced by the presence of CaP and CaOx crystals in the LOH and calyx region of our kidney tissues respectively. To support our observation of tissue calcification, we performed Von Kossa staining of WTT and KOT kidneys (Fig. 6D) and performed gene expression of known calcification markers. Gene expression of bone morphogenic proteins (BMPs) namely;

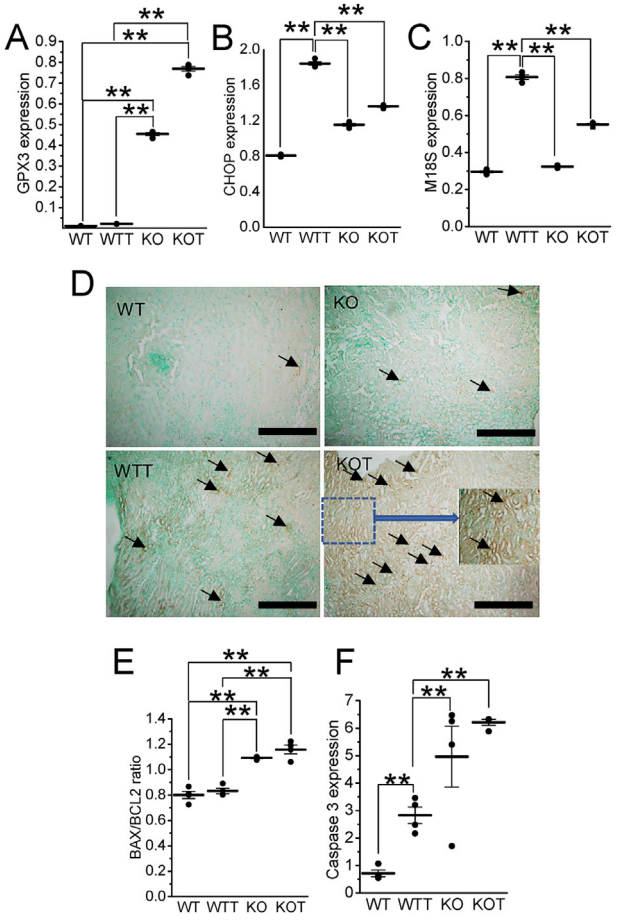

Figure 8 Induced-hypercalciuria increases oxidative stress in PT cells and give rise to ER stress-induced apoptosis. Evidence of ER-stress induced apoptosis with ROS generation and oxidative stress in PT cells. **(A)** Expression of GPX3 gene, as marker for protection of oxidative stress, quantitated in PT cells from WT, WT CaG-treated (WTT), TRPC3 KO (KO), and KO CaG-treated (KOT) is significantly higher in the KOT group compared to all other groups. Evidence of ER stress following CaG treatment is shown through gene expressions for **(B)** CHOP and **(C)** M18S, markers for ER stress, assessed for WT, WTT, KO, and KOT mice PT cells. Histological evidence of apoptosis in kidneys through **(D)** Annexin V staining of WT, WTT, KO, and KOT sagittal kidney sections to assess apoptotic regions in kidney tissue; image shows LOH regions with black arrows pointing to apoptotic regions. Genetic assessment of apoptotic markers **(E)** BAX/BCL2 ratio and **(F)** Caspase 3 are significantly higher for the treated groups especially for KOT compared to the controls. Kidneys for sectioning or RT-PCR were obtained were obtained from $n = 4$ mice of each group (WT, WTT, KO, and KOT); all gene expressions were normalized to GAPDH. Scatter plot quantifications in **(A–F)** are means ± SEM *, $P < 0.05$; **, $P < 0.01$. Black bars = 100 μm.

BMP-2, BMP-6, BMP-7, were significantly higher in our WTT and KOT groups compared to controls (Fig. 6E–G), while osteocalcin 2 (OCL-2), osteopontin 4 (OPN-4), and Runt-related transcription factor 2 (RUNX2) also showed similar trends as the BMPs (Fig. 6H–J). It should be noted that KOT exhibited a more pronounced effect of calcification (Fig. 6B–I), suggesting that TRPC3 plays an important role in PT luminal Ca^{2+} clearance when exposed to higher tubular [Ca^{2+}] *in vivo*.

Inflammatory and fibrotic genes were upregulated in CaG treated group

Observations from our lab and other groups[43,44] suggest that the pathological calcification can be accompanied by other pathophysiological conditions, such as inflammation and fibrosis.[44,45] We observed more widespread range of apparent fibrotic areas (Masson's staining) in the kidneys of KOT groups compared to the WT counterpart (Fig. 7A), notably the cortical and medullary areas of the kidney, indicating higher degrees of inflammation. To provide support, we examined the expression of fibrotic marker genes such as Transforming Growth Factor Beta 1 (TGF-β1), Fibronectin 1 (FN-1), and alpha smooth muscle actin (SMα) in PT cells from CaG-treated mice[46,47] and found that treated groups show an upregulation of fibrotic markers, particularly in absence of TRPC3 (Fig. 7B–D). We also investigated the degree of kidney damage due to hypercalciuric conditions in kidney sections, which revealed histological fragmentations in both WTT and KOT groups in the cortical areas of the kidney, with the KOT mice section showing the most fragmentation (Fig. 7E). As expected, genetic expression levels for inflammation markers [NLRP3, Interleukins (IL): IL-1β, IL-6, MCP1 and NF-κβ] were also shown to be significantly increased in CaG-treated mice compared to their untreated counterpart (Fig. 7F–J).[48,49] NF-κβ–NLRP3–IL-1β signaling pathway can be activated during stone formation; thus IL-1β, a known potent inducer of TGF-β1 and IL-6,[46–48] stimulates fibrotic and inflammatory processes. In addition, both IL-6 and TGF-β1 have been recognized as important molecules to induce pathological calcification via interplay with BMP-2.[9,50]

TRPC3 KO kidney in hypercalciuric can lead to greater apoptosis in PT

Association of fibrosis and inflammation are found in pathological conditions that promote apoptosis.[51] Resulting conditions due to higher Ca^{2+} in PT cells may drive the apoptotic response due to ROS generation and oxidative stress. Therefore, we examined the expression of Glutathione peroxidase 3 (GPX3), an oxidative stress protection gene,[52] which exhibited significant upregulation in the *TRPC3* KO groups than all the other groups tested (Fig. 8A). It is worth noting that the rise in GPX3 expression in the KOT group could be an action by KOT PT cells to offset the rise in ROS productions by adjusting ROS to homeostatic levels, possibly due to KOT PT cells being more affected by oxidative stress induced by hypercalciuric conditions than WTT PT cells, which would explain the differences observed among the treated groups. Furthermore, previous studies have provided evidence of a NF-κβ pathway link with ER-stress-induced apoptosis.[53] ER-stress genes C/EBP homologous protein (CHOP) and M18S were assessed in the extracted PT cells.[54] Expressions of CHOP and M18S in WTT and KOT groups were greater compared to respective WT and KO groups (Fig. 8B, C), suggesting that greater renal

Ca^{2+} loads conditions can elicit PT cell ER-stress. To confirm that the hypercalciuric group experienced greater apoptosis, an *in-situ* apoptosis assay (which specifically binds to fragmented DNA and stains it brown) was performed on kidney tissues. Results of which signified that the control groups had very little apoptotic activity, but both WTT and KOT groups experienced a significant increase in area-specific apoptosis (Fig. 8D). These observations were further supported by examining apoptotic marker gene expression [(B-cell lymphoma 2 (BCL2), BCL2 Associated X (BAX), and Caspase 3], which showed upregulated BAX/BCL2 ratio and Caspase 3 expression in the treatment groups, particularly in KOT PT cells (Fig. 8E, F), making the KOT group more susceptible to cell death. In fact, such condition can provide cell debris for aggregation and growth of calcium stone.[10]

Discussion

Since elevated filtrate [Ca^{2+}], due to deletion of TRPC3, could not represent the human-like pathology of CaNL, our effort was to further raise the luminal $[Ca^{2+}]_o$ in mild hypercalciuric *TRPC3* KO mice. Importantly, formation of CaP crystals in LOH is the predisposing factor for CaP and mixed stone formation,[12,13,18] which was present in our *TRPC3* KO mice.[17] Thus, by increasing the $[Ca^{2+}]_o$ at the tubular lumen through supplemental calcium ingestion in *TRPC3* KO mice, we tried to create a predisposing condition for CaP crystal formation, seeking to establish the role of such condition to produce a more human-like CaNL phenotype. Our results in KOT PT cells suggest that TRPC3 is not merely a channel involved in Ca^{2+} reabsorption; its absence may further mediate calcium crystal formation due to CaG treatment. While our previous study found CaSR-TRPC3 mediated transcellular Ca^{2+} transport pathway comprised of calbindins, PMCA and NCX in mice PT cells,[17] CaG treatment did not change the expression of those proteins of transcellular machinery in mice PT cells (Fig. S4). The observed upregulation in CaSR function, may then be caused by greater CaSR activity and sensitivity to Ca^{2+} uptake in WTT PT cells, whereas in KOT, such activity was significantly compromised to accommodate increased luminal [Ca^{2+}]. Furthermore, elevated filtrate [Ca^{2+}] cannot be properly handled without the coordination of TRPC3. Thus, the stagnated Ca^{2+} transport in those PT cells, passing higher $[Ca^{2+}]_o$ downstream that goes through the LOH, can generate CaP crystals. Further downstream from distal tubule interaction, this may induce mixed crystal formation.[55]

We do acknowledge that the mice we used in our study are global *TRPC3* KO mice. However, while TRPC3 is present in other parts of the nephron,[56] the PT handles most of the Ca^{2+} transport.[16] On the other hand, the regulation of renal tubular [Ca^{2+}] by TRPV5/V6 has been shown in distal convoluted tubule and TAL, which are, however, much smaller compared to PT and downstream from the site of initial CaP crystal formation (LOH).[4] Therefore, transcellular Ca^{2+} transport in PT can significantly reduce the chance of CaP crystal formation at LOH, since the most common metabolic abnormality found in calcium stone formers is hypercalciuria, as seen in idiopathic hypercalciuria,[18] which is PTH-independent.[57] While CaSR-TRPC3 pathway activation sensitivity can be modulated by L-Phe, a closer look at the receptor activations after CaG treatment yielded interesting results. First, our data suggest that TRPC3 can have a crucial role in regulating $[Ca^{2+}]_o$ in CaG-induced hypercalciuric conditions because of increased TRPC3 current for adjusting the PT luminal $[Ca^{2+}]_o$. Second, in WTT PT cells, TRPC3 activity may be upregulated to account for the increased luminal $[Ca^{2+}]_o$; however, hypercalciuria may be compromising both TRPC3 and CaSR functioning. Indeed, KOT PT cells can be more accommodative in CaSR functioning, which shows the distinctive role of CaSR and TRPC3 in PT Ca^{2+} handling in hypercalciuric conditions. Since our recent study found that in normal PT cells ROCE is the major physiological pathway of Ca^{2+} entry in murine PT cells,[17] our results with induced-hypercalciuric conditions have shown that Ca^{2+} entry in PT cells switched to SOCE mode, as we have seen in ROS-induced human PT cells.[9] Delineating the CaSR-TRPC3 pathway during such hypercalciuric environment in WT mice Ca^{2+} entry pathway became more accommodative to engage more Ca^{2+} via CaSR activation, thus more SOCE. Similar finding has been shown in defective SOCE to cause nephrogenic diabetes insipidus, where compromised SOCE markedly diminishes AQP2 abundance in CD cells.[35]

Although the PO_4^{3-} concentration appears to be inversely correlated to the excretion of the amount of Ca^{2+}, the urinary PO_4^{3-} differences, when compared to the WT and KO groups, became exacerbated after CaG treatment, suggesting the formation of CaP may correlate with the decline in PO_4^{3-}.[43] CaG treatments generated CaP + CaOx crystals suggesting that additional $[Ca^{2+}]_o$ may be necessary for such mixed stone formation. Urine from WTT/KOT mice showed presence of urine cells with calcified materials, an effect of which was more pronounced in KOT. Since these cells are PT in origin, PT epithelial lining damage due to CaG treatment has become apparent. Since significant PT cellular damage are indicative of ROS production, which is also vital to the pathogenesis of stone formation, our assessment of oxidative stress and LDH release in urine of WTT and KOT mice demonstrate overall tubular function compromise, which essentially progressed the renal damage and stone formation. Calcium crystals are the factors in cell death and ROS production[9,10]; specifically, damaged PT cells could provide membranous substrates for CaP + CaOx crystal nucleation and their aggregation in the downstream segments of the nephron.[42] Since the ablation of TRPC3 (KOT) exacerbates these conditions, TRPC3 could have a protective role against crystal formation and renal damage by extracting PT $[Ca^{2+}]_o$ via Ca^{2+} influx into PT cells.

Our findings provide a link between hypercalciuric conditions and exacerbation of renal fibrosis and inflammation particularly in absence of TRPC3. All inflammatory markers we tested (IL-1β, IL-6, MCP1 and NF-κβ, NLRP3) supports our idea of a connection between inflammation and hypercalciuria. Studies have shown that crystal uptake triggers innate immune activation via the secretion of IL-1β to revise the pathogenesis of crystal-related disorders, where intracellular NLRP3 inflammasome acts as a pattern recognition platform to trigger inflammation and acute kidney injury (AKI) in oxalate nephropathy.[58] Our proof of concept, study introducing the NLRP3 inflammasome

potentially the mechanisms driving crystalline nephropathies that maybe associated with CaP crystals. Similar findings of activation of NLRP3 have been demonstrated in dendritic cells, which is however, independent of $[Ca^{2+}]_i$ rise.[59] Similarly, the increased expression of fibrotic markers namely TGF-β1, FN-1 and SMα all of which also shows a link between hypercalciuria and renal fibrosis. Concurrent upregulation of both fibrotic and inflammatory genes amongst the treated groups, suggests that hypercalciuric stress may have exerted immune axis to provide a protective role in renal fibrosis. Notably, NLRP3 has some protective effect in renal fibrosis which is supported by knocked down or inhibited condition.[60–62] Such process of activation can possibly compensate for the rise in renal fibrosis following hypercalciuric conditions, depending on the results of the future study along this line.

Our study is relevant to the clinical supplementation of calcium,[21] including post-menopausal conditions in women,[22] where longer-term usage of calcium supplement, viz. CaG, can develop pathologies through prolonged hypercalciuric stress. Thus, exploring the cellular and molecular events of such effect in kidney tubule, specifically when PT Ca^{2+} transport has been compromised, is relevant to understand the pathophysiology. In fact, PT cells are particularly most vulnerable to oxidative damage due to excessive ROS generation.[63,64] Such stress response due to fluctuations of extracellular Ca^{2+} can trigger oxidative damage, causing cellular injury,[10,65] leading to various pathophysiological conditions[66–68] e.g., inflammation, fibrosis, and/or apoptosis, which can contribute to acute or chronic kidney diseases.[9,10,68,69] We have evidence that excessive $[Ca^{2+}]_i$ via CaSR-activated SOCE can lead to ER-stress[9] (live cell ER-tracker activity; Fig. S5A) and ROS production[68] (H2DCFDA fluorescence; Fig. S5B) in TRPC3 ablated PT cells. Thus, augmented hypercalciuric conditions could impact CaSR-driven oxidative stress in PT cells, where TRPC3 may have protective role. This can be used as a direct mechanistic link between hypercalciuria, and ER stress and ROS production, because such downstream activities were diminished by CaSR inhibitor, NPS-2143.

Conclusion

Hypercalciuria is a major metabolic anomaly in CaNL, and by disrupting Ca^{2+} transport in KOT PT cells, we were able to show the resultant increase in CaP crystal formation, which may have further increased the CaP + CaOx mixed crystal formation. Our results provide a significant associative evidence of the deleterious effects of prolonged hypercalciuria and its implication in the pathogenesis and development of mixed urine crystal formation. Moreover, increase in $[Ca^{2+}]_i$ through Ca^{2+}-signaling to induce ER-stress and Caspase activation[70] in WTT and KOT PT cells can be implicated in apoptosis under hypercalciuric conditions, where KOT groups are more susceptible, thus substantiating the pivotal role of TRPC3 in PT cells in the kidney injury pathogenesis and the development of kidney stones. The sustained Ca^{2+} entry in PT cells leads to the stagnation of $[Ca^{2+}]_i$ and the detrimental processes that causes PT cell death. Such process generates material such as cellular debris, which can bind with the CaP and CaP + CaOx crystals already formed in the downstream tubular lumen to help in growth and aggregation of those crystals to create stones. Our understanding of the role of TRPC3 in stone-forming pathway activation can pave the way towards developing therapeutic strategies.

Author contributions

Conception and design: B. C. B., S. S., C. L. I., E. A. B., S. K. R. and B. C.; Acquisition and analysis (e.g., statistical analysis) of experimental data: C. L. I., S. S., B. C., E. A. B. and S. K. R.; Interpretation of data: B. C. B., C. L. I., S. S., B. C., E. A. B. and S. K. R.; Writing the manuscript draft, review and revision of the manuscript: C. L. I., S. S., B. C., E. A. B., S. K. R. and B. C. B. Funding acquisition: B. C. B.

Conflict of interests

The authors declare that there is no conflict of interests.

Funding

National Institute of Diabetes and Digestive and Kidney Diseases (No. DK102043) funding to B.C.B supported this study. There was no involvement of those funding agencies in the preparation of this manuscript, design, collection, analyses, and interpretation of the data, writing of the report, and/or decision to submit this article for publication.

Acknowledgements

We would like to thank Calcium Signaling Lab members Farai C. Gombedza, Gireesh Subramaniam, Samuel Yeroushalmi and Yianni L. Kanaras for helping in some experiments and data analysis.

Data accessibility

The data that support the findings of this study are available from the corresponding author upon reasonable request.

Appendix A. Supplementary data

Supplementary data to this article can be found online at https://doi.org/10.1016/j.gendis.2021.04.006.

References

1. Romero V, Akpinar H, Assimos DG. Kidney stones: a global picture of prevalence, incidence, and associated risk factors. *Rev Urol*. 2010;12(2–3):e86–e96.
2. Carbone A, Al Salhi Y, Tasca A, et al. Obesity and kidney stone disease: a systematic review. *Minerva Urol Nefrol*. 2018;70(4):393–400.
3. Bird VY, Khan SR. How do stones form? Is unification of theories on stone formation possible? Cómo se forman las piedras? *Arch Esp Urol*. 2017;70(1):12–27.

4. Evan AP, Lingeman JE, Coe FL, et al. Randall's plaque of patients with nephrolithiasis begins in basement membranes of thin loops of Henle. *J Clin Invest*. 2003;111(5):607—616.
5. Bushinsky DA. Nephrolithiasis: site of the initial solid phase. *J Clin Invest*. 2003;111(5):602—605.
6. Lieske JC, Farell G, Deganello S. The effect of ions at the surface of calcium oxalate monohydrate crystals on cell-crystal interactions. *Urol Res*. 2004;32(2):117—123.
7. Hammes MS, Lieske JC, Pawar S, Spargo BH, Toback FG. Calcium oxalate monohydrate crystals stimulate gene expression in renal epithelial cells. *Kidney Int*. 1995;48(2):501—509.
8. Sun XY, Ouyang JM, Yu K. Shape-dependent cellular toxicity on renal epithelial cells and stone risk of calcium oxalate dihydrate crystals. *Sci Rep*. 2017;7(1):7250.
9. Gombedza FC, Shin S, Kanaras YL, Bandyopadhyay BC. Abrogation of store-operated Ca2+ entry protects against crystal-induced ER stress in human proximal tubular cells. *Cell Death Discov*. 2019;5:124.
10. Gombedza F, Evans S, Shin S, et al. Melamine promotes calcium crystal formation in three-dimensional microfluidic device. *Sci Rep*. 2019;9(1):875.
11. He Z, Jing Z, Jing-Cun Z, Chuan-Yi H, Fei G. Compositional analysis of various layers of upper urinary tract stones by infrared spectroscopy. *Exp Ther Med*. 2017;14(4):3165—3169.
12. Tiselius HG. A hypothesis of calcium stone formation: an interpretation of stone research during the past decades. *Urol Res*. 2011;39(4):231—243.
13. Asplin JR, Mandel NS, Coe FL. Evidence of calcium phosphate supersaturation in the loop of Henle. *Am J Physiol*. 1996;270(4 Pt 2):F604—F613.
14. Parks JH, Coward M, Coe FL. Correspondence between stone composition and urine supersaturation in nephrolithiasis. *Kidney Int*. 1997;51(3):894—900.
15. Wagner CA, Mohebbi N. Urinary pH and stone formation. *J Nephrol*. 2010;23(Suppl 16):S165—S169.
16. Friedman PA. Mechanisms of renal calcium transport. *Exp Nephrol*. 2000;8(6):343—350.
17. Ibeh CL, Yiu AJ, Kanaras YL, et al. Evidence for a regulated Ca2+ entry in proximal tubular cells and its implication in calcium stone formation. *J Cell Sci*. 2019;132(9):jcs225268.
18. Coe FL, Worcester EM, Evan AP. Idiopathic hypercalciuria and formation of calcium renal stones. *Nat Rev Nephrol*. 2016;12(9):519—533.
19. Curhan GC, Willett WC, Rimm EB, Stampfer MJ. A prospective study of dietary calcium and other nutrients and the risk of symptomatic kidney stones. *N Engl J Med*. 1993;328(12):833—838.
20. Favus MJ. The risk of kidney stone formation: the form of calcium matters. *Am J Clin Nutr*. 2011;94(1):5—6.
21. Krause M, Keller J, Beil B, et al. Calcium gluconate supplementation is effective to balance calcium homeostasis in patients with gastrectomy. *Osteoporos Int*. 2015;26(3):987—995.
22. Epstein O, Kato Y, Dick R, Sherlock S. Vitamin D, hydroxyapatite, and calcium gluconate in treatment of cortical bone thinning in postmenopausal women with primary biliary cirrhosis. *Am J Clin Nutr*. 1982;36(3):426—430.
23. Hartmann J, Dragicevic E, Adelsberger H, et al. TRPC3 channels are required for synaptic transmission and motor coordination. *Neuron*. 2008;59(3):392—398.
24. Kim SJ, Kwon SK, Kim HY, Kim SM, Bae JW, Choi JK. DPP-4 inhibition enhanced renal tubular and myocardial GLP-1 receptor expression decreased in CKD with myocardial infarction. *BMC Nephrol*. 2019;20(1):75.
25. Zhuo JL, Li XC, Garvin JL, Navar LG, Carretero OA. Intracellular ANG II induces cytosolic Ca2+ mobilization by stimulating intracellular AT1 receptors in proximal tubule cells. *Am J Physiol Renal Physiol*. 2006;290(6):F1382—F1390.
26. Bandyopadhyay BC, Swaim WD, Sarkar A, Liu X, Ambudkar IS. Extracellular Ca(2+) sensing in salivary ductal cells. *J Biol Chem*. 2012;287(36):30305—30316.
27. Bandyopadhyay BC, Pingle SC, Ahern GP. Store-operated Ca2+ signaling in dendritic cells occurs independently of STIM1. *J Leukoc Biol*. 2011;89(1):57—62. Epub 2010 Oct 22.
28. Paul H, Reginato AJ, Schumacher HR. Alizarin red S staining as a screening test to detect calcium compounds in synovial fluid. *Arthritis Rheum*. 1983;26(2):191—200.
29. Suchý P, Straková E, Herzig I, Staňa J, Kalusová R, Pospíchalová M. Toxicological risk of melamine and cyanuric acid in food and feed. *Interdiscip Toxicol*. 2009;2(2):55—59.
30. Shin S, Gombedza FC, Bandyopadhyay BC. l-ornithine activates Ca^{2+} signaling to exert its protective function on human proximal tubular cells. *Cell Signal*. 2020;67:109484.
31. Thompson ME, Lewin-Smith MR, Kalasinsky VF, et al. Characterization of melamine-containing and calcium oxalate crystals in three dogs with suspected pet food-induced nephrotoxicosis. *Vet Pathol*. 2008;45(3):417—426.
32. Meimaridou E, Lobos E, Hothersall JS. Renal oxidative vulnerability due to changes in mitochondrial-glutathione and energy homeostasis in a rat model of calcium oxalate urolithiasis. *Am J Physiol Renal Physiol*. 2006;291(4):F731—F740.
33. Kos CH, Karaplis AC, Peng JB, et al. The calcium-sensing receptor is required for normal calcium homeostasis independent of parathyroid hormone. *J Clin Invest*. 2003;111(7):1021—1028.
34. Kamiyama M, Garner MK, Farragut KM, Kobori H. The establishment of a primary culture system of proximal tubule segments using specific markers from normal mouse kidneys. *Int J Mol Sci*. 2012;13(4):5098—5111.
35. Mamenko M, Dhande I, Tomilin V, et al. Defective store-operated calcium entry causes partial nephrogenic diabetes insipidus. *J Am Soc Nephrol*. 2016;27(7):2035—2048.
36. Ueda N, Mayeux PR, Walker PD, Shah SV. Receptor-mediated increase in cytosolic calcium in LLC-PK1 cells by platelet activating factor and thromboxane A2. *Kidney Int*. 1991;40(6):1075—1081.
37. Kiyonaka S, Kato K, Nishida M, et al. Selective and direct inhibition of TRPC3 channels underlies biological activities of a pyrazole compound. *Proc Natl Acad Sci U S A*. 2009;106(13):5400—5405.
38. Armato U, Chiarini A, Chakravarthy B, et al. Calcium-sensing receptor antagonist (calcilytic) NPS 2143 specifically blocks the increased secretion of endogenous Aβ42 prompted by exogenous fibrillary or soluble Aβ25-35 in human cortical astrocytes and neurons-therapeutic relevance to Alzheimer's disease. *Biochim Biophys Acta*. 2013;1832(10):1634—1652.
39. Schleifer H, Doleschal B, Lichtenegger M, et al. Novel pyrazole compounds for pharmacological discrimination between receptor-operated and store-operated Ca(2+) entry pathways. *Br J Pharmacol*. 2012;167(8):1712—1722.
40. Merritt JE, Armstrong WP, Benham CD, et al. SK&F 96365, a novel inhibitor of receptor-mediated calcium entry. *Biochem J*. 1990;271(2):515—522.
41. Kukkonen JP, Lund PE, Akerman KE. 2-aminoethoxydiphenyl borate reveals heterogeneity in receptor-activated Ca(2+) discharge and store-operated Ca(2+) influx. *Cell Calcium*. 2001;30(2):117—129.
42. Tsujihata M. Mechanism of calcium oxalate renal stone formation and renal tubular cell injury. *Int J Urol*. 2008;15(2):115—120.
43. Evan AP, Lingeman JE, Coe FL, et al. Crystal-associated nephropathy in patients with brushite nephrolithiasis. *Kidney Int*. 2005;67(2):576—591.
44. Lau I, Potluri A, Ibeh CL, Redman RS, Paal E, Bandyopadhyay BC. Microcalcifications in stone-obstructed human submandibular gland are associated with apoptosis and cell proliferation. *Arch Oral Biol*. 2017;82:99—108.

45. Palit S, Kendrick J. Vascular calcification in chronic kidney disease: role of disordered mineral metabolism. *Curr Pharm Des*. 2014;20(37):5829—5833.
46. Luo DD, Fielding C, Phillips A, Fraser D. Interleukin-1 beta regulates proximal tubular cell transforming growth factor beta-1 signalling. *Nephrol Dial Transplant*. 2009;24(9):2655—2665.
47. Vesey DA, Cheung CW, Cuttle L, Endre ZA, Gobé G, Johnson DW. Interleukin-1 beta induces human proximal tubule cell injury, alpha-smooth muscle actin expression and fibronectin production. *Kidney Int*. 2002;62(1):31—40.
48. Vilaysane A, Chun J, Seamone ME, et al. The NLRP3 inflammasome promotes renal inflammation and contributes to CKD. *J Am Soc Nephrol*. 2010;21(10):1732—1744.
49. Grandaliano G, Gesualdo L, Bartoli F, et al. MCP-1 and EGF renal expression and urine excretion in human congenital obstructive nephropathy. *Kidney Int*. 2000;58(1):182—192.
50. Huang RL, Sun Y, Ho CK, et al. IL-6 potentiates BMP-2-induced osteogenesis and adipogenesis via two different BMPR1A-mediated pathways. *Cell Death Dis*. 2018;9(2):144.
51. Portilla D. Apoptosis, fibrosis and senescence. *Nephron Clin Pract*. 2014;127(1—4):65—69.
52. Olson GE, Whitin JC, Hill KE, et al. Extracellular glutathione peroxidase (Gpx 3) binds specifically to basement membranes of mouse renal cortex tubule cells. *Am J Physiol Renal Physiol*. 2010;298(5):F1244—F1253.
53. Zhu X, Huang L, Gong J, et al. NF-κB pathway link with ER stress-induced autophagy and apoptosis in cervical tumor cells. *Cell Death Discov*. 2017;3:17059.
54. Szegezdi E, Logue SE, Gorman AM, Samali A. Mediators of endoplasmic reticulum stress-induced apoptosis. *EMBO Rep*. 2006;7(9):880—885.
55. Tiselius HG, Lindbäck B, Fornander AM, Nilsson MA. Studies on the role of calcium phosphate in the process of calcium oxalate crystal formation. *Urol Res*. 2009;37(4):181—192.
56. Goel M, Sinkins WG, Zuo CD, Estacion M, Schilling WP. Identification and localization of TRPC channels in the rat kidney. *Am J Physiol Renal Physiol*. 2006;290(5):F1241—F1252.
57. Loupy A, Ramakrishnan SK, Wootla B, et al. PTH-independent regulation of blood calcium concentration by the calcium-sensing receptor. *J Clin Invest*. 2012;122(9):3355—3367.
58. Mulay SR, Evan A, Anders HJ. Molecular mechanisms of crystal-related kidney inflammation and injury. Implications for cholesterol embolism, crystalline nephropathies and kidney stone disease. *Nephrol Dial Transplant*. 2014;29(3):507—514.
59. Katsnelson MA, Rucker LG, Russo HM, Dubyak GR. K+ efflux agonists induce NLRP3 inflammasome activation independently of Ca2+ signaling. *J Immunol*. 2015;194(8):3937—3952.
60. Kim SM, Kim YG, Kim DJ, et al. Inflammasome-independent role of NLRP3 mediates mitochondrial regulation in renal injury. *Front Immunol*. 2018;9:2563.
61. Gong W, Mao S, Yu J, et al. NLRP3 deletion protects against renal fibrosis and attenuates mitochondrial abnormality in mouse with 5/6 nephrectomy. *Am J Physiol Renal Physiol*. 2016;310(10):F1081—F1088.
62. Anders HJ, Suarez-Alvarez B, Grigorescu M, et al. The macrophage phenotype and inflammasome component NLRP3 contributes to nephrocalcinosis-related chronic kidney disease independent from IL-1-mediated tissue injury. *Kidney Int*. 2018;93(3):656—669.
63. Bhargava P, Schnellmann RG. Mitochondrial energetics in the kidney. *Nat Rev Nephrol*. 2017;13(10):629—646.
64. Hall AM, Unwin RJ, Parker N, Duchen MR. Multiphoton imaging reveals differences in mitochondrial function between nephron segments. *J Am Soc Nephrol*. 2009;20(6):1293—1302.
65. Chen B, Li Y, Liu Y, Xu Z. circLRP6 regulates high glucose-induced proliferation, oxidative stress, ECM accumulation, and inflammation in mesangial cells. *J Cell Physiol*. 2019;234(11):21249—21259.
66. Mai X, Shang J, Liang S, et al. Blockade of Orai 1 store-operated calcium entry protects against renal fibrosis. *J Am Soc Nephrol*. 2016;27(10):3063—3078.
67. Pinton P, Giorgi C, Siviero R, Zecchini E, Rizzuto R. Calcium and apoptosis: ER-mitochondria Ca2+ transfer in the control of apoptosis. *Oncogene*. 2008;27(50):6407—6418.
68. Yiu AJ, Ibeh CL, Roy SK, Bandyopadhyay BC. Melamine induces Ca^{2+}-sensing receptor activation and elicits apoptosis in proximal tubular cells. *Am J Physiol Cell Physiol*. 2017;313(1):C27—C41.
69. Ratliff BB, Abdulmahdi W, Pawar R, Wolin MS. Oxidant mechanisms in renal injury and disease. *Antioxid Redox Signal*. 2016;25(3):119—146.
70. Chen S, He FF, Wang H, et al. Calcium entry via TRPC6 mediates albumin overload-induced endoplasmic reticulum stress and apoptosis in podocytes. *Cell Calcium*. 2011;50(6):523—529.